Stability of Electrodynamic Maglev Vehicles Propelled by Permanent-Magnet Linear Electric Motors

Salvatore Circosta[1]*, Renato Galluzzi[2], Andrea Tonoli[1], Nicola Amati[1], Angelo Bonfitto[1], Torbjörn A. Lembke[3], and Milan Kertész[3]

[1] Department of Mechanical and Aerospace Engineering, Politecnico di Torino
Corso Duca degli Abruzzi 24, 10129 Turin, Italy
salvatore.circosta@polito.it
andrea.tonoli@polito.it
nicola.amati@polito.it
angelo.bonfitto@polito.it

[2] School of Engineering and Sciences, Tecnologico de Monterrey
Calle del Puente 222, 14380 Mexico City, Mexico
renato.galluzzi@tec.mx

[3] HyperloopTT
135 Avenue du Comminges, 31270 Cugnaux, France
torbjorn.lembke@hyperlooptt.com
milan.kertesz@hyperlooptt.com

Abstract

The search for fast and efficient transportation systems has raised the interest in magnetic levitation technologies over the last decades. In this context, the Hyperloop concept has been conceived as a solution for future mobility. However, the stability of the electrodynamic levitation system represents a key enabling technology for the Hyperloop implementation. In this context, the state of the art has addressed the full stabilization of downscaled vehicles, where levitation and guidance are provided by electrodynamic means. This is achieved passively by introducing a proper amount of damping into the system. Nevertheless, this system stability could be affected when using permanent-magnet propulsion motors. In this perspective, we propose the stabilization of a downscaled vehicle under the influence of its propulsion system. To this end, a permanent-magnet linear synchronous motor is designed. Its stiffness contribution is evaluated and introduced into the vehicle model. Then, its impact on the stability and performance of the system is discussed in detail.

1 Introduction

In the last decades, the mobility paradigm has received a strong innovative push. Globalization and environmental concerns have driven the transport industry towards the search for sustainable, efficient, fast, and safe systems. Worldwide governments strongly support this trend through programs aimed at funding research in this field [1, 2].

In this framework, the Hyperloop concept has been conceived as a breakthrough solution for future mobility [3]. Based on Robert Goddard's vactrain [4], it features magnetically levitated capsules traveling inside a low-pressure tube under the propulsion of linear electric motors [5]. This enables cruise speeds up to 1200 km/h and an ideal zero-emission feature. Recently,

*Corresponding author.

several companies have focused on the development and implementation of Hyperloop. The academic community has also been involved in this effort through direct collaborations with these companies or through student teams participating in the SpaceX Hyperloop Pod Competition.

The magnetic levitation of Hyperloop relies on the Inductrack technology [6]. It uses the electrodynamic principle, where lift and drag force components originate from the interaction between capsule-mounted permanent magnets and a conducting track yields. Electrodynamic levitation perfectly suits very high-speed applications since it features increasing lift and decreasing drag forces as the speed escalates. Other appealing features of this technology are its fully passive layout, the large air gaps attained through levitation, its self-reliability, simplicity and low component count.

The electrodynamic phenomenon has been widely studied in the past for electrodynamic bearings (EDBs). The literature proposes different EDB configurations and modeling approaches. Simulations and experimentation have identified the unstable nature of this principle [7, 8, 9, 10, 11]. In fact, its interaction with the mechanical domain is intrinsically unstable and requires the addition of damping for stabilization purposes.

Post *et al.* first proposed the application of electrodynamic levitation to translational systems in the Inductrack project frame [6, 12, 13]. As its rotating counterpart, linear motion levitation is unstable. This was observed during an experimental campaign with a full-scale prototype [14, 15], where increasing vertical vibrations were limited by safety auxiliary wheels.

Extensive work has dealt with the modeling and identification of the electrodynamic forces [16, 17, 18, 19, 20, 21, 22, 23, 24]. Although these efforts have proposed experimentation and diverse modeling approaches, stability issues for systems of translational nature have been often oversimplified and not treated properly. Furthermore, the stabilization of such systems was not properly addressed.

To close this gap, Galluzzi *et al.* proposed a multidomain lumped-parameter modeling approach that reproduces the strong interaction between electrical and mechanical dynamics [25]. The unstable nature was identified and tackled by introducing passive damping through a secondary suspension. Nevertheless, the work dealt only with the stabilization of the vertical dynamics of a quarter-car system.

Stable operation of every degree of freedom (DOF) is required for the successful implementation of systems featuring full electrodynamic levitation. In this perspective, a subsequent effort by Circosta *et al.* addressed the full stabilization of a downscaled vehicle, where levitation and guidance are provided by electrodynamic means [26].

Although the latest works pose a solid base for the future implementation of systems levitated through electrodynamic means, they investigate and address stability without accounting for the propulsion system. The latter consists of a linear electric motor that could introduce stiffness contributions along the degrees of freedom of the levitated system. Consequently, the stability of the system could be affected.

In this context, the present work addresses the stability of a downscaled vehicle under the influence of its propulsion system. The proposed vehicle is taken from reference [26] and enhanced with a permanent-magnet linear synchronous motor (PMLSM). Furthermore, system performance is investigated in terms of electrodynamic drag.

Although numerous Hyperloop proposals focus on the use of linear induction machines, a PMLSM solution has been proposed by Gurol *et al.* [15]. PMLSMs offer greater force capability, larger power factor and reduced overheating problems when compared to induction machines. However, they pose a challenge in terms of stability because they introduce significant stiffness contributions in the vehicle DOFs.

The remainder of this work is structured as follows. Section 2 describes the system layout.

Section 3 discusses the modeling of the system. At first, the electric machine is modeled and designed to fulfill required performance. Then, its stiffness contributions on the vehicle degrees of freedom are evaluated and included in the system model. Section 4 presents the system performance assessment in terms of stability and electrodynamic drag. Finally, Section 5 concludes the work.

2 System layout

The retained system (Fig. 1) is derived from Circosta *et al.* [26], where the sprung and unsprung bodies are connected by four secondary suspensions, and the unsprung body is equipped with four levitation (vertical) and four guidance (lateral) pads. The described configuration is enhanced with a permanent-magnet linear synchronous motor (PMLSM) added to the unsprung body to provide propulsion force.

The geometrical dimensions of the different bodies are set to roughly reproduce the track and wheelbase of a Hyperloop Pod Competition vehicle [27]. The height of the vehicle is considered relatively short when compared to the other dimensions.

The levitation and guidance pads are located at the four corners of the body: the former are mounted on the bottom of the unsprung body, whereas the latter appear on its sides. As in [26], the pad consists of a Halbach array of NdFeB permanent magnets (PM) interacting with a continuous aluminum slab that follows the track specifications of the Hyperloop Pod Competition [28].

The secondary suspension provides stiffness and damping in the vertical (z) and lateral (y) directions. Conversely, the suspension is infinitely rigid in the longitudinal direction (x). The secondary suspension is simplified as a prismatic joint acting independently along each direction. Its positioning and stiffness features were defined to set the natural frequencies of the sprung body in the range 1.2 to 1.44 Hz. Damping features were derived from an optimization procedure aimed at maximizing overall system stability in terms of a root locus [26].

The general layout of the electric machine is taken from [29], where a linear induction machine features the stator mounted on the pod. To worsen system stability, we replaced the linear induction machine with a PMLSM. It presents a magnetic rail which is magnetized by N45SH-grade NdFeB PMs, and a stator with two magnetic circuits (left and right) and three-phase windings. The former is fixed to the track, the latter is placed on the bottom of the unsprung body. The centroid of the stator's active part is located at a vertical offset (z direction) of 60 mm with respect to the unsprung body's center of gravity (COG).

The geometrical and inertial features along with the secondary suspension parameters of the retained system are reported in Table 1.

3 Modeling

The proposed system travels along the x direction with speed v. For each body, the translation DOFs y (sway) and z (heave) along with the rotation DOFs around x axis (roll, ϕ), y axis (pitch, θ) and z axis (yaw, ψ) are investigated. The dynamics of the translation DOF x is not considered.

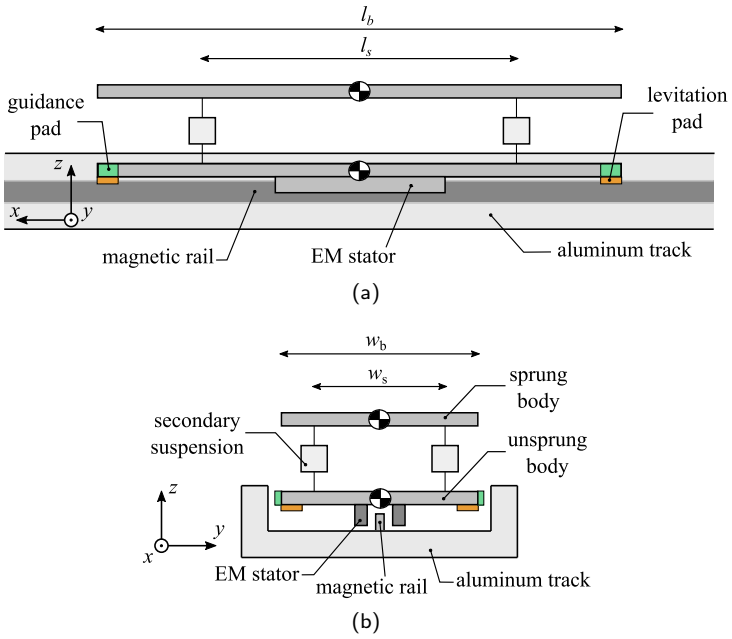

Figure 1: System layout: (a) side view and (b) front view

Table 1: Geometrical and inertial features of the system

	Feature	Symbol	Value	Unit
Secondary suspension	Positioning x	l_{s}	1732	mm
	Positioning y	w_{s}	416	mm
	Stiffness y	$k_{\mathrm{s,y}}$	1.137	kN/m
	Stiffness z	$k_{\mathrm{s,z}}$	1.137	kN/m
	Damping y	$c_{\mathrm{s,y}}$	265.3	Ns/m
	Damping z	$c_{\mathrm{s,z}}$	262.7	Ns/m
Sprung and unsprung bodies	Length	l_{b}	2500	mm
	Width	w_{b}	600	mm
Sprung body*	Mass	m_{s}	80	kg
	Moment of inertia x	$I_{\mathrm{s,x}}$	2.40	$\mathrm{kg \cdot m^2}$
	Moment of inertia y	$I_{\mathrm{s,y}}$	41.67	$\mathrm{kg \cdot m^2}$
	Moment of inertia z	$I_{\mathrm{s,z}}$	44.07	$\mathrm{kg \cdot m^2}$
Unsprung body*	Mass	m_{u}	8	kg
	Moment of inertia x	$I_{\mathrm{u,x}}$	0.24	$\mathrm{kg \cdot m^2}$
	Moment of inertia y	$I_{\mathrm{u,y}}$	4.17	$\mathrm{kg \cdot m^2}$
	Moment of inertia z	$I_{\mathrm{u,z}}$	4.41	$\mathrm{kg \cdot m^2}$

* Inertial properties are referred to the body center of gravity

3.1 Permanent-Magnet Linear Synchronous Motor

To yield a propulsion force to the proposed vehicle, a PMLSM was custom-sized. For versatility, a single elementary segment is proposed.

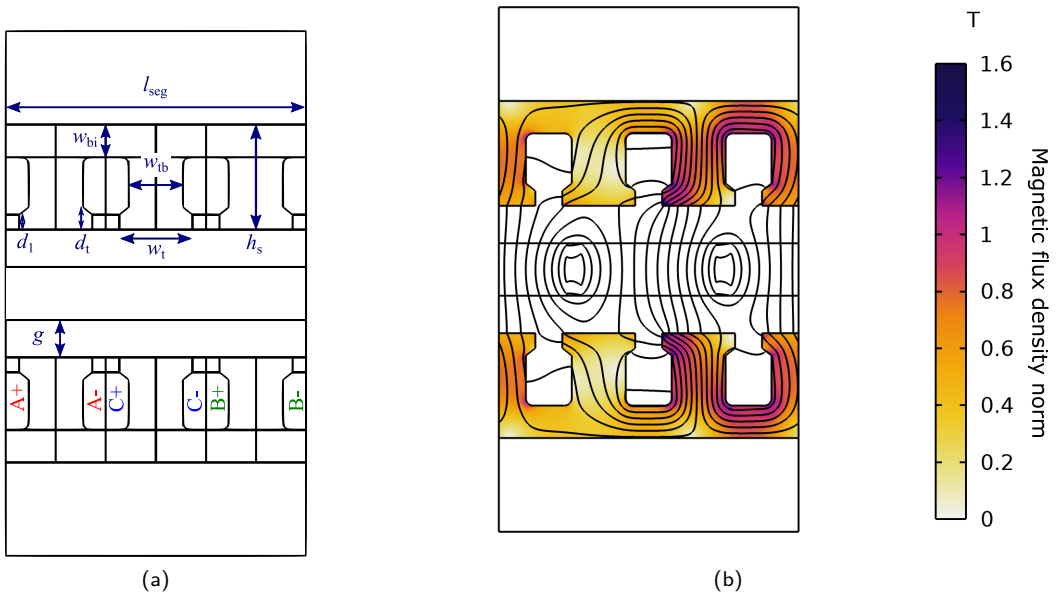

Figure 2: On-board stator of the permanent-magnet linear synchronous motor: 2D view of (a) geometric features and (b) finite-element model results in terms of stator magnetic flux density norm (color map) and out-of-plane magnetic vector potential contours. Windings are fed by a root-mean-square three-phase current density of $6\,\mathrm{A/mm^2}$.

Table 2: Permanent-magnet linear synchronous motor parameters

Feature	Symbol	Value	Unit
Segment length	l_{seg}	200	mm
Segment nominal force	F_{seg}	400	N
Back iron width	w_{bi}	21.67	mm
Tooth base width	w_{tb}	36	mm
Tooth tip width	w_t	48.67	mm
Shoe tip height	d_1	10	mm
Shoe total height	d_t	5	mm
Stator height	h_s	70	mm
Nominal propulsion air gap	g	25	mm
Active length	l_{act}	30	mm

Figure 2 illustrates the layout of a single PMLSM segment, which consists of two symmetrical on-board stator cores made of soft iron and a part of the magnetic rail which is magnetized by N45SH-grade PMs. Both stators have three-phase concentrated windings to reduce end-turn length. In nominal conditions, the magnetic rail is perfectly centered with respect to the stator structures with a nominal air gap g.

A design procedure was followed to establish the geometry of the proposed electric machine. It consists in selecting the proper back iron and tooth dimensions to maximize propulsion forces while avoiding magnetic saturation. Thereafter, parameters listed in Table 2 are obtained, thus leading to a segment able to yield 400 N of propulsion force.

Given the total mass of the vehicle (88 kg), a propulsion force of 2 kN is needed to attain a

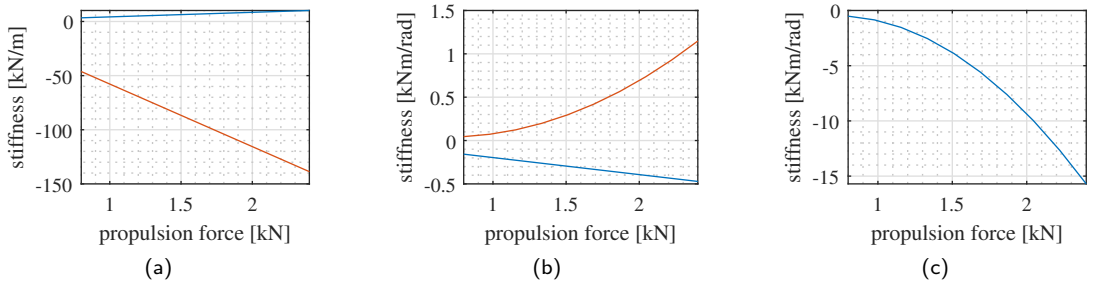

Figure 3: Linear permanent-magnet synchronous motor stiffness terms as a function of the propulsion force: (a) heave (blue) and sway (orange); (b) roll (blue) and pitch (orange); (c) yaw.

stall acceleration of 2.4 g. These specifications comply with those of a prototype competing at the Hyperloop Pod Competition [30]. To achieve this force output, the magnetic rail must be adapted with the necessary poles. The designed segment with two poles is able to provide a propulsion force of 400 N, thus, ten poles or five segments are needed to attain 2 kN.

The interaction among ferromagnetic and PM domains will inevitably yield additional force and torque components. Specifically, efforts will arise in relevant degrees of freedom: heave, sway, roll, pitch and yaw. From a modeling perspective, these contributions can be represented as stiffness parameters—positive or negative—depending on the degree of freedom of interest. They are evaluated through 3D finite-element models. Moreover, these simulations can be repeated for different propulsion forces, which can be obtained by varying the length of the magnetic rail. This yields the sensitivity of elastic effects to motor force capability. Results for all the relevant stiffness terms (k_{heave} k_{sway} k_{roll} k_{pitch} k_{yaw}) are presented in Fig. 3. Do note that these contributions can be changed also by changing the active length of the PMLSM. However, $l_{\text{act}} = 30$ mm is required for optimal operation within the levitation air gaps of interest, so this parametric variation was not explored herein.

The motor provides negative stiffness contributions to the sway, yaw and roll DOFs, thus affecting system stability in these dynamics. Conversely, it provides positive stiffening effects to the heave and pitch DOFs.

3.2 System model

The state-space representation reported in [26] is used to model the entire system. The electrodynamic levitation principle is represented through a multi-domain lumped parameter approach, first proposed by [25]. After proper tuning, this model is able to reproduce the desired electrodynamic characteristic at a small fraction of the computational cost needed in a more complex finite-element simulation.

In the following, the problem is formulated for a generic pad. The electrical parallel of N_{b} branches reproduces the dynamic behavior of the current path inside the track conductor. Each branch features specific resistance and inductance values. For the kth branch, the electrical circuit is governed by

$$\frac{\mathrm{d}i_{\mathrm{d},k}}{\mathrm{d}t} = -\omega_{\mathrm{p},k} i_{\mathrm{d},k} + \omega i_{\mathrm{q},k} - \frac{1}{L_k}\frac{\partial \Lambda}{\partial q_{\mathrm{p}}}\dot{q}_{\mathrm{p}} \tag{1}$$

$$\frac{\mathrm{d}i_{\mathrm{q},k}}{\mathrm{d}t} = -\omega_{\mathrm{p},k} i_{\mathrm{q},k} - \omega i_{\mathrm{d},k} - \frac{1}{L_k}\Lambda\omega \tag{2}$$

where i_{d} and i_{q} are the direct- and quadrature-axis current components, q_{p} is the generic-pad air gap, $\omega_{\mathrm{p},k} = R_k/L_k$ the electromagnetic pole frequency, and R_k and L_k the branch resistance and inductance, respectively. The pad longitudinal speed v and the mechanical frequency are linked through the pole pitch ratio of the PM array γ:

$$\omega = \frac{v}{\gamma} \tag{3}$$

The Λ term denotes the amplitude of the PM array flux linkage acting on the track lumped coils.It is an exponential function of the air gap [6]:

$$\Lambda = \Lambda_0 \mathrm{e}^{-\frac{q_{\mathrm{p}}}{\gamma}} \tag{4}$$

being Λ_0 the flux linkage constant.

When N_{b} circuit branches superimpose, lift and drag force components are written as

$$F_{\mathrm{lift}} = \frac{\partial \Lambda}{\partial q_{\mathrm{p}}} \sum_{k=1}^{N_{\mathrm{b}}} i_{\mathrm{d},k} \tag{5}$$

$$F_{\mathrm{drag}} = -\frac{\Lambda}{\gamma} \sum_{k=1}^{N_{\mathrm{b}}} i_{\mathrm{q},k} \tag{6}$$

At constant air gap q_{p} and longitudinal speed v, lift and drag static forces are obtained from the combination Eqs. 1,2, 5 and 6:

$$F_{\mathrm{lift},0} = \frac{\Lambda_0^2}{\gamma} \mathrm{e}^{-\frac{2q_{\mathrm{p}}}{\gamma}} \sum_{k=1}^{N_{\mathrm{b}}} \frac{\omega^2/\omega_{\mathrm{p},k}^2}{L_k\left(1+\omega^2/\omega_{\mathrm{p},k}^2\right)} \tag{7}$$

$$F_{\mathrm{drag},0} = \frac{\Lambda_0^2}{\gamma} \mathrm{e}^{-\frac{2q_{\mathrm{p}}}{\gamma}} \sum_{k=1}^{N_{\mathrm{b}}} \frac{\omega/\omega_{\mathrm{p},k}}{L_k\left(1+\omega^2/\omega_{\mathrm{p},k}^2\right)} \tag{8}$$

The levitation pads feature the layout proposed by Post [12]. For this configuration, the lumped-parameter modeling approach was proposed by Galluzzi *et al.* [25], who demonstrated a feasible set of parameters with $N_{\mathrm{b}} = 3$ branches (Table 3). The subscript l refers to the levitation pad.

As in [26], the guidance pads are a scaled version of the levitation ones, where the width is scaled by a factor $\beta = 0.75$. The flux linkage constant, the inductance and the resistance of the

Table 3: Levitation pad parameters

Feature	Symbol	Value	Unit
Branch pole frequency	$\omega_{\mathrm{p},1}$ $\omega_{\mathrm{p},2}$ $\omega_{\mathrm{p},3}$	355.45 $2.57 \cdot 10^3$ $1.73 \cdot 10^4$	rad/s
Branch inductance	$L_{1,\mathrm{l}}$ $L_{2,\mathrm{l}}$ $L_{3,\mathrm{l}}$	$7.72 \cdot 10^{-10}$ $2.06 \cdot 10^{-9}$ $4.12 \cdot 10^{-9}$	H
Flux linkage constant	$\Lambda_{0,\mathrm{l}}$	0.33	mWb
Pole pitch ratio	γ	15.9	mm

kth branch are derived from the levitation pad parameters as follows:

$$\Lambda_{0,\mathrm{g}} = \beta \Lambda_{0,\mathrm{l}} \tag{9}$$

$$R_{k,\mathrm{g}} = \beta R_{k,\mathrm{l}} \tag{10}$$

$$L_{k,\mathrm{g}} = \beta L_{k,\mathrm{l}} \tag{11}$$

where subscript g refers to the guidance pad.

Each pad of the system is represented through Eqs. 1, 2, 5 and 6 by replacing the generic-pad air gap (q_{p}) with the levitation-pad (z_{l}) or the guidance-pad (y_{g}) air gaps along with the respective pad parameters. The air gaps are expressed as a linear combination of the unsprung body DOFs by following geometrical considerations.

Lift and drag forces enter the equations of motion of the unsprung body, thus coupling the electrical and mechanical domains. The electrodynamic levitation description is nonlinear. By following the analytical approach developed in [26], the above-reported equations are linearized around the air gap value $q_{0,\mathrm{p}}$. It is expressed as $z_{0,\mathrm{l}}$ and $y_{0,\mathrm{g}}$ for the levitation and guidance pads, respectively.

The levitation pads counteract the weight of the system. Hence, they undergo an imposed constant load. The air gap adapts to guarantee static equilibrium between the weight and the lift forces, as discussed in [25]. Hence, such value is obtained by matching the total lift to the total weight of the system. Four pads work in parallel in this case, hence:

$$z_{0,\mathrm{l}}(\omega) = -\frac{\gamma}{2} \ln \left(\frac{(m_{\mathrm{s}} + m_{\mathrm{u}}) \mathrm{g} \gamma}{4 \Lambda_{0,\mathrm{l}}^2 \Gamma_{\mathrm{l}}(\omega)} \right) \tag{12}$$

On the other hand, the air gap of the guidance pads is controlled to have a pad equivalent stiffness $k_{\mathrm{eq,g}}$, as discussed in [26]. According to the reference, the air gap that satisfies this constraint is given by

$$y_{0,\mathrm{g}}(\omega) = -\frac{\gamma}{2} \ln \left(\frac{k_{\mathrm{eq,g}} \gamma^2}{2 \Lambda_{0,\mathrm{g}}^2 \Gamma_{\mathrm{g}}(\omega)} \right) \tag{13}$$

The linearized electrodynamic description is introduced in the mechanical equations of motion. The latter relies on the assumption that the pitch, yaw and roll dynamics are decoupled. Hence, the three systems with reduced number of DOFs—heave-pitch, sway-yaw and heave-

sway-roll—are defined. Finally, the obtained description is arranged into the state-space form.

For the sake of brevity, the full description along with the state-space dynamic matrices are skipped. The reader can find this information in reference [26]. However, when compared to the referred configuration, dynamic matrices of the present formulation must be updated to account for the electric motor stiffness contributions. Accordingly, the following elements are modified:

$$[A_{\mathrm{m},1}]_{8\times 8} \quad \begin{cases} a_{1,2} = -\frac{4k_{\mathrm{s,z}}}{m_{\mathrm{u}}} - \frac{k_{\mathrm{heave}}}{m_{\mathrm{u}}} \\ a_{3,4} = -\frac{k_{\mathrm{s,z}} l_{\mathrm{s}}^2}{I_{\mathrm{u,y}}} - \frac{k_{\mathrm{pitch}}}{I_{\mathrm{u,y}}} \end{cases} \tag{14}$$

$$[A_{\mathrm{m},2}]_{8\times 8} \quad \begin{cases} a_{1,2} = -\frac{4k_{\mathrm{s,y}}}{m_{\mathrm{u}}} - \frac{k_{\mathrm{sway}}}{m_{\mathrm{u}}} \\ a_{3,4} = -\frac{k_{\mathrm{s,y}} l_{\mathrm{s}}^2}{I_{\mathrm{u,z}}} - \frac{k_{\mathrm{yaw}}}{I_{\mathrm{u,z}}} \end{cases} \tag{15}$$

$$[A_{\mathrm{m},3}]_{12\times 12} \quad \begin{cases} a_{1,2} = -\frac{4k_{\mathrm{s,z}}}{m_{\mathrm{u}}} - \frac{k_{\mathrm{heave}}}{m_{\mathrm{u}}} \\ a_{3,4} = -\frac{4k_{\mathrm{s,y}}}{m_{\mathrm{u}}} - \frac{k_{\mathrm{sway}}}{m_{\mathrm{u}}} \\ a_{5,6} = -\frac{k_{\mathrm{s,z}} w_{\mathrm{s}}^2}{I_{\mathrm{u,x}}} - \frac{k_{\mathrm{roll}}}{I_{\mathrm{u,x}}} \end{cases} \tag{16}$$

where $A_{\mathrm{m},j}$ [26] are the mechanical sub-matrices whose sub-index j refers to the particular model: heave-pitch ($j = 1$), sway-yaw ($j = 2$) and heave-sway-roll ($j = 3$) models. The added stiffness terms of the PMLSM have been already defined in Sec. 3.1.

4 Results and discussion

4.1 System stability

The state-space description reported in Section 3.2 is used to assess system stability. To this end, the linearization air gaps—$z_{0,\mathrm{l}}$ and $y_{0,\mathrm{g}}$ for the levitation and guidance pads, respectively—are computed through Eqs. 12 and 13, respectively. The latter is defined to set the sway natural frequency of the unsprung body $\omega_{\mathrm{n,su}} \cong 15 \cdot \omega_{\mathrm{n,ss}}$, being $\omega_{\mathrm{n,ss}}$ the sway natural frequency of the sprung body [26]. The unsprung body is constrained by four secondary suspensions and four pads. Furthermore, it must compensate for the electric motor stiffness k_{sway}. Hence, the required equivalent stiffness of the guidance pad is given by

$$k_{\mathrm{eq,g}} = \frac{1}{4}\left(\omega_{\mathrm{n,su}}^2 m_{\mathrm{u}} - 4k_{\mathrm{s,y}} - k_{\mathrm{sway}}\right) \tag{17}$$

Figure 4 shows the linearization air gap for the levitation (dashed) and guidance (solid) pads. The latter depends on the sway stiffness contribution of the motor and, consequently, on its size. As the motor negative stiffness increases, the guidance pads must provide larger positive stiffness, thus leading to thinner guidance air gaps. At speed values below 0.89 m/s, the levitation pads are not sufficient to balance the vehicle weight. Therefore, a backup system is needed during take-off and landing operations. The same occurs for the guidance pads: they cannot provide the required stiffness below speed values ranging from 1.05 m/s to 1.44 m/s, according to the motor size.

Then, the poles of the three analytical models (Sec. 3.2) are calculated at different longitudinal speeds and motor sizes. To this end, the eigenvalues of the state matrices (Eqs. 15,16 and 16) are computed. Within the whole speed range, the pole with the largest real part is

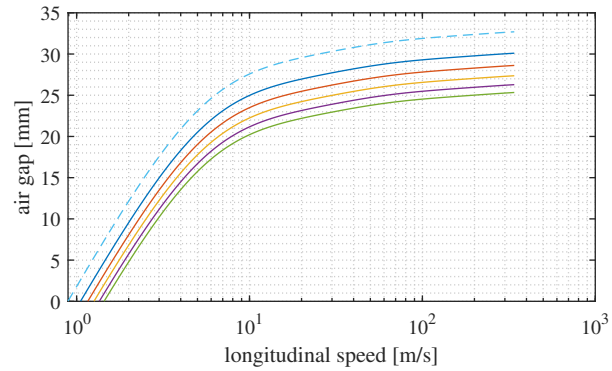

Figure 4: Air gap as function of the longitudinal speed: levitation (dashed) and guidance (solid) pads. The latter is a function of the propulsion force: 800 N (blue), 1200 N (orange), 1600 N (yellow), 2000 N (purple) and 2400 N (green).

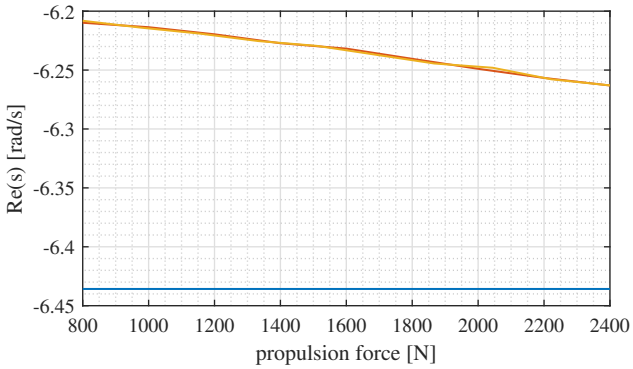

Figure 5: Real part of the most stable pole as function of the propulsion force: heave-pitch (blue), sway-yaw (orange) and heave-sway-roll (yellow) models.

identified and its real part is plotted against the motor force capability, which is proportional to its size. These results are depicted in Fig. 5 for the heave-pitch, sway-yaw, and heave-sway-roll models.

The sway-yaw and heave-sway-roll models have superimposed trends. Hence, they feature the same poles with largest real part, namely the sway ones. The motor stiffness contribution has little influence on the system stability therein. As shown in [26], the poles with largest real part are related to the sprung body dynamics. These are almost decoupled to the unsprung body ones, as the natural frequencies of the two bodies are at least one decade apart. This is achieved thanks to the secondary suspension design [26] and the guidance-pad air gap. The latter is fundamental for the system stability since it must compensate for the sway negative stiffness. Otherwise, sway poles of the unsprung body would move to lower frequency bands, couple with the sprung body dynamics and push the system to instability.

4.2 Drag force assessment

In this section, the drag force due to the electrodynamic levitation system is evaluated to assess the propulsion performance. Four levitation and four guidance pads contribute to the total drag

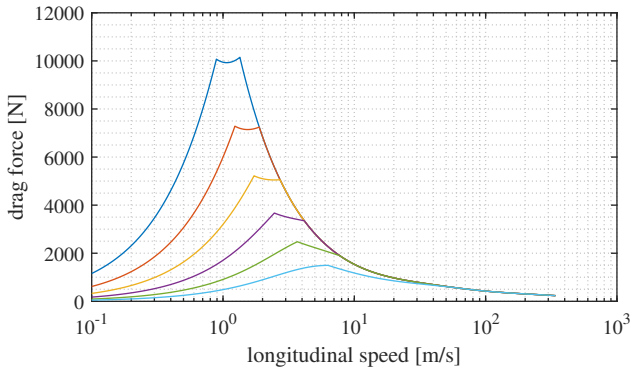

Figure 6: Total drag as a function of the longitudinal speed when the air gap is low-bounded at 0 mm (blue), 5 mm (orange), 10 mm (yellow), 15 mm (purple), 20 mm (green) and 25 mm (cyan).

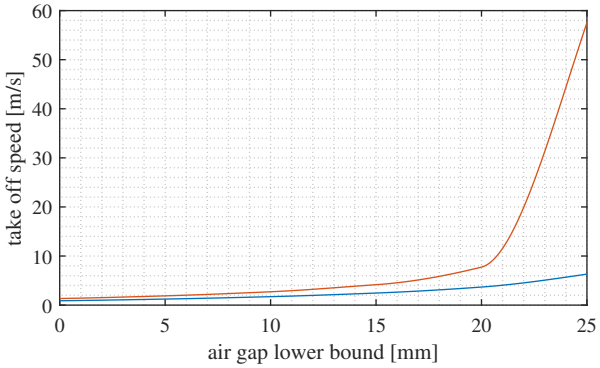

Figure 7: Take-off speed as a function of the air gap lower bound for the levitation (blue) and guidance (orange) pads.

according to Eq. 8. This expression is a function of the longitudinal speed and the linearization air gaps, i.e. equations 12 and 13. The latter is influenced by the motor stiffness contribution according to Eq. 17. For demonstration purposes, the following analysis considers the stiffness contribution given by a motor force capability of 2 kN.

Figure 6 shows the total drag when the air gap profile is bounded at values ranging from 0 to 25 mm. This is achieved by means of a backup-wheel system that provides levitation and guidance during take-off and landing operations. The motor force capability (2 kN) must be larger than the total drag to guarantee available force to accelerate the vehicle at 2.4g. Thereby, the air gap must be bounded to at least 25 mm.

The take-off speed is the value at which the electrodynamic lift is sufficient to counteract the vehicle weight (levitation pads) or provide sufficient guidance stiffness (guidance pads). Above this speed value, the backup-wheel system can be retracted. In this condition, the vehicle relies totally on electrodynamic lift.

Figure 7 shows the take-off speed for the levitation and guidance pads as function of the air gap lower bound. As the latter increases, the speed needed to develop sufficient electrodynamic lift increases.

A take-off speed of 57.5 m/s for the guidance pads occurs when the air gap is limited to a minimum of 25 mm. The latter is required to guarantee available force to accelerate the

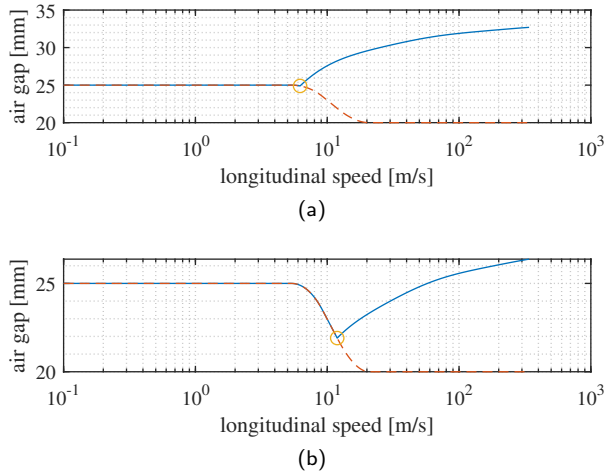

Figure 8: Actual (solid) and lower-bound (dashed) air gap profiles as a function of the longitudinal speed: (a) levitation and (b) guidance pads. The circle indicates the take-off point.

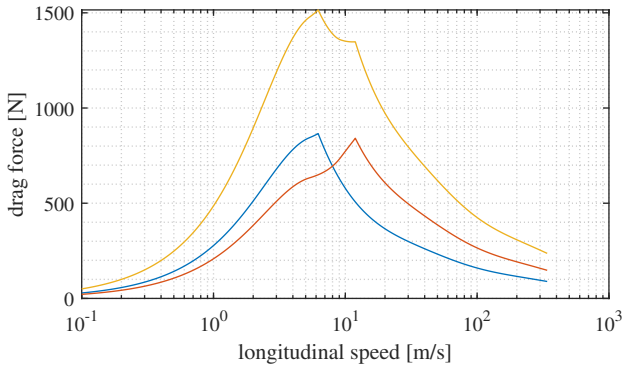

Figure 9: Drag force as function of the speed when the lower-bound air gap profile is imposed: total drag (yellow), levitation (blue) and guidance (orange) pads contribution.

vehicle. Large take-off speed values imply constraints on the design of the backup-wheel system. To this end, its value can be decreased by defining a suitable profile for the air gap lower bound. Specifically, the air gap is low-bounded to 25, mm at speed values below the speed that corresponds to the maximum drag force. Afterwards, the air gap lower bound is gradually decreased, as shown in Figs. 8a and 8b (dashed profile). By doing so, the take-off speed of the guidance pad is decreased to 11.9 m/s.

Figure 9 shows the drag force when the above-mentioned lower-bound profile of the air gap is imposed. Specifically, the levitation and guidance pads contribution, and the total drag are displayed. The latter is always smaller than the motor force (2 kN), thus guaranteeing sufficient propulsion.

5 Conclusions

The present paper dealt with the stability and performance assessment of downscaled vehicles levitated through electrodynamic means under the influence of permanent-magnet linear electric motors. The retained vehicle was taken from the literature and integrated with a permanent-magnet linear synchronous motor for propulsion.

To this end, the propulsion motor was custom-sized to fulfill a target stall acceleration. Then, its stiffness contributions to the vehicle DOFs were assessed through 3D finite-element simulations. Moreover, these simulations were repeated for different motor sizes to evaluate the sensitivity of such stiffness effects to motor force capability. As result, the motor provides stabilizing effect to the heave and pitch DOFs. Conversely, it contributes with negative stiffness to the sway, yaw and roll dynamics.

The stiffness contributions were included into the model of the system. The air gap of the guidance pads was set to compensate for the motor destabilizing effect. The system stability was investigated by extracting the poles of the linearized model. Specifically, the pole with largest real part was found at diverse motor sizes. Despite the stiffness contributions, the system was demonstrated to be stable thanks to the secondary suspension design and the selection of a suitable air gap for the guidance pads.

Finally, the propulsion performance of the system was assessed. As demonstrated, the peak electrodynamic drag must be limited to guarantee sufficient propulsion. To this end, the air gap was low-bounded and a suitable limit profile was proposed and validated.

References

[1] Michael E. Webber. Electric Highway. *Mechanical Engineering*, 141(06):32–37, 2019.

[2] Luisa Marelli, Anastasios Tsakalidis, Konstantinos Gkoumas, Anwar Haq, Monica Grosso, and Ferenc Pekar. Strategic transport research and innovation agenda (STRIA) roadmap factsheets, 2017.

[3] Konstantinos Gkoumas. Hyperloop Academic Research: A Systematic Review and a Taxonomy of Issues. *Applied Sciences*, 11(13):5951, June 2021.

[4] Natalie Burkhard. Why invent the Hyperloop?, 2014.

[5] Kenneth Decker, Jeffrey Chin, Andi Peng, Colin Summers, Golda Nguyen, Andrew Oberlander, Gazi Sakib, Nariman Sharifrazi, Christopher Heath, Justin Gray, and Robert Falck. Conceptual Feasibility Study of the Hyperloop Vehicle for Next-Generation Transport. page 22, Jan. 2017.

[6] R. F. Post and D. Ryutov. The Inductrack concept: A new approach to magnetic levitation. Technical Report UCRL-ID-124115, Lawrence Livermore National Lab., CA (United States), May 1996.

[7] Torbjörn A. Lembke. *Design and analysis of a novel low loss homopolar electrodynamic bearing*. PhD thesis, School of Electrical Engineering, KTH, Stockholm, Sweden, 2005.

[8] Andrea Tonoli, Nicola Amati, Fabrizio Impinna, and Joaquim Girardello Detoni. A Solution for the Stabilization of Electrodynamic Bearings: Modeling and Experimental Validation. *Journal of Vibration and Acoustics*, 133(2):021004, 2011.

[9] Joachim Van Verdeghem, Virginie Kluyskens, and Bruno Dehez. Stability and Performance Analysis of Electrodynamic Thrust Bearings. *Actuators*, 8(1):11, March 2019.

[10] J. Van Verdeghem, V. Kluyskens, and B. Dehez. Five degrees of freedom linear state-space representation of electrodynamic thrust bearings. *Journal of Sound and Vibration*, 405:48–67, September 2017.

[11] A.V. Filatov and E.H. Maslen. Passive magnetic bearing for flywheel energy storage systems. *IEEE Transactions on Magnetics*, 37(6):3913–3924, November 2001.

[12] R. F. Post. Inductrack demonstration model. Technical Report UCRL-ID-129664, Lawrence Livermore National Lab., CA (United States), February 1998.

[13] R.F. Post and D.D. Ryutov. The Inductrack: a simpler approach to magnetic levitation. *IEEE Transactions on Appiled Superconductivity*, 10(1):901–904, 2000.

[14] Husam Gurol, Robert Baldi, Phillip Jeter, In-Kun Kim, Daryl Bever, and General Atomics. General atomics low speed maglev technology development program (Supplemental# 3). Technical report, United States. Federal Transit Administration. Office of Technology, 2005.

[15] Sam Gurol and Bob Baldi. Overview of the General Atomics Urban Maglev Technology Development Program. In *Proceedings of the 2004 IEEE/ASME Joint Rail Conference*, pages 187–191, Baltimore, MD, USA, 04 2004.

[16] Hitoshi Tsunashima and Masato Abe. Static and dynamic performance of permanent magnet suspension for maglev transport vehicle. *Vehicle System Dynamics*, 29(2):83–111, 1998.

[17] O.F. Storset and B. Paden. Infinite dimensional models for perforated track electrodynamic magnetic levitation. In *Proceedings of the 41st IEEE Conference on Decision and Control, 2002.*, volume 1, pages 842–847, Las Vegas, NV, USA, 2002. IEEE.

[18] Roshan Pradhan and Aditya Katyayan. Vehicle dynamics of permanent-magnet levitation based Hyperloop capsules. In *ASME 2018 Dynamic Systems and Control Conference*, page V002T22A004, Atlanta, GA, USA, 2018.

[19] J Íñiguez and V Raposo. Laboratory scale prototype of a low-speed electrodynamic levitation system based on a Halbach magnet array. *European Journal of Physics*, 30(2):367–379, March 2009.

[20] TS Indraneel, Vignesh Jayakumar, Abhishek Soni, Dhaval R Shiyani, Kanishk Tyagi, and Shabaan Abdallah. Levitation array testing for Hyperloop pod design. In *AIAA Scitech 2019 Forum*, page 0787, San Diego, CA, USA, 2019.

[21] Guo, Li, and Zhou. Study of a Null-Flux Coil Electrodynamic Suspension Structure for Evacuated Tube Transportation. *Symmetry*, 11(10):1239, October 2019.

[22] Yin Chen, Wenlong Zhang, Jonathan Z. Bird, Subhra Paul, and Kunlun Zhang. A 3-D Analytic-Based Model of a Null-Flux Halbach Array Electrodynamic Suspension Device. *IEEE Transactions on Magnetics*, 51(11):1–5, November 2015.

[23] Jiaheng Duan, Song Xiao, Kunlun Zhang, Mihai Rotaru, and J. K. Sykulski. Analysis and Optimization of Asymmetrical Double-Sided Electrodynamic Suspension Devices. *IEEE Transactions on Magnetics*, 55(6):1–5, June 2019.

[24] Ruiyang Wang and Bingen Yang. A Transient Model of Inductrack Dynamic Systems. In *Volume 8: 31st Conference on Mechanical Vibration and Noise*, page V008T10A062, Anaheim, California, USA, August 2019. American Society of Mechanical Engineers.

[25] Renato Galluzzi, Salvatore Circosta, Nicola Amati, Andrea Tonoli, Angelo Bonfitto, Torbjörn A. Lembke, and Milan Kertész. A Multi-domain Approach to the Stabilization of Electrodynamic Levitation Systems. *Journal of Vibration and Acoustics*, pages 1–30, 2020.

[26] Salvatore Circosta, Renato Galluzzi, Nicola Amati, Andrea Tonoli, Angelo Bonfitto, Torbjörn A Lembke, and Milan Kertész. Passive Multi-Degree-of-Freedom Stabilization of Ultra-High-Speed Maglev Vehicles. *Journal of Vibration and Acoustics*, page 13.

[27] M. M. J. Opgenoord, C. Merian, J. Mayo, P. Kirschen, C. O'Rourke, G. Izatt, et al. MIT Hyperloop final report. Technical report, Massachusetts Institute of Technology, Cambridge, Massachusetts, 2017.

[28] SpaceX. SpaceX Hyperloop test-track specification, 2016.

[29] Available online: https://swissloop.ch/prototypes/.

[30] Available online: https://tumhyperloop.de/hyperloop-prototypes.